

## Far-Infrared [C II] Line Survey Observations of the Galactic Plane

Takao Nakagawa, Yukari Yamashita Yui<sup>1</sup>, Yasuo Doi<sup>2</sup>, Haruyuki Okuda,  
Hiroshi Shibai<sup>3</sup>, and Kenji Mochizuki<sup>4</sup>

The Institute of Space and Astronautical Science,  
Yoshinodai 3-1-1, Sagamihara, Kanagawa 229, Japan

and

Tetsuo Nishimura<sup>5</sup> and Frank J. Low  
Steward Observatory, University of Arizona, Tucson, AZ 85721

### ABSTRACT

We present results of our survey observations of the [C II] 158  $\mu\text{m}$  line emission from the Galactic plane using the Balloon-borne Infrared Carbon Explorer (BICE). Our survey covers a wide area ( $350^\circ \lesssim l \lesssim 25^\circ$ ,  $|b| \lesssim 3^\circ$ ) with a spatial resolution of  $15'$ . We employed a new observing method called the “fast spectral scanning” to make large-scale observations efficiently.

Strong [C II] line emission was detected from almost all areas we observed. In the general Galactic plane, the spatial distribution of the [C II] line emission correlates very well with that of far-infrared continuum emission, but diffuse components are more prominent in the [C II] line emission; the  $I_{[\text{CII}]} / I_{\text{FIR}}$  ratio is  $\sim 0.6\%$  for diffuse components but is  $\sim 0.2\%$  for compact sources such as active star-forming regions. In the Galactic center region, on the other hand, the distribution of the [C II] line emission is quite different from that of the far-infrared continuum emission, and the  $I_{[\text{CII}]} / I_{\text{FIR}}$  ratio is systematically lower there.

The FWHM velocity resolution of our instrument is  $175 \text{ km s}^{-1}$ , but we determined the central velocity of the line at each observed point very precisely with statistical

---

<sup>1</sup>Present Address: Communications Research Laboratory, Nukui-kitamachi 4-2-1, Koganei, Tokyo 184, Japan

<sup>2</sup>Present Address: Department of Earth Science and Astronomy, University of Tokyo, Komaba 3-8-1, Meguro-ku, Tokyo 153, Japan

<sup>3</sup>Present Address: Department of Astrophysics, Nagoya University, Furo-cho, Chikusa-ku, Nagoya 464-01, Japan

<sup>4</sup>Present Address: Department of Astronomy, University of Texas at Austin, Austin, TX 78712-1083

<sup>5</sup>Present Address: National Astronomical Observatory, Osawa 2-21-1, Mitaka, Tokyo 181, Japan

errors as small as  $\pm 6$  km s<sup>-1</sup>. The longitudinal distribution of the central velocity clearly shows the differential rotation pattern of the Galactic disk and also violent velocity fields around the Galactic center.

*Subject headings:* Galaxy: General – infrared: interstellar: lines – ISM: Clouds

## 1. INTRODUCTION

The far-infrared [C II] fine structure line ( ${}^2P_{3/2} \rightarrow {}^2P_{1/2}$ , 157.7409  $\mu\text{m}$ , Cooksy, Blake, & Saykally 1986) has been predicted to be the dominant coolant of neutral interstellar gas (e.g., Dalgarno & McCray 1972), and is expected to determine the cooling rate (and consequently the temperature) of general interstellar clouds. This is because (1) the C atom is easily ionized by general interstellar radiation field, since its ionization energy (11.3 eV) is lower than that of H atom (13.6 eV), and (2) the C<sup>+</sup> ion is easily excited collisionally from its ground level ( ${}^2P_{1/2}$ ) to the first fine-structure level ( ${}^2P_{3/2}$ ) due to its relatively small energy difference ( $\Delta E/k = 91$  K) and to its small critical density ( $n_{\text{cr}} = 3 \times 10^3$  cm<sup>-3</sup> for H I). Hence the line is expected to be a useful probe of the energy budget of general interstellar gas. Moreover, since the [C II] line is very bright, its observations can trace general interstellar clouds on a large scale, and hence can reveal the global structure of the Galaxy.

The [C II] line cannot be observed from the ground because of heavy absorption due to atmospheric water vapor. Thus most of previous observations have been made from the Kuiper Airborne Observatory (KAO) (see, e.g., Haas, Davidson, & Erickson 1995) or from balloon-borne telescopes (e.g., Matsuhara et al. 1989, Shibai et al. 1991, and Mizutani et al. 1994). Most of these observations were restricted to small areas around active star-forming regions or to active regions in starburst galaxies. Since, in these regions, interstellar clouds are directly exposed to very strong ultraviolet radiation from young OB stars, photodissociation region models with rather intense radiation field and high density gas (e.g., Tielens & Hollenbach 1985) have been successfully applied to interpret the observations.

The clouds in these active regions, however, do not represent general clouds in the Galaxy, and most of interstellar clouds in the Galaxy have lower gas density and are exposed to much weaker radiation field. Hence large-scale [C II] line survey observations of various kinds of interstellar clouds are required to reveal general characteristics of interstellar clouds in the Galaxy. Moreover, since the total emission from ordinary galaxies is dominated by emission from these general clouds, large-scale [C II] line observations of the Galaxy are also important to our understanding of interstellar clouds in other galaxies.

Few observations of large-scale [C II] line emission from the Galaxy have been made so far. The pioneering observations by Stacey et al. (1985) using an air-borne telescope and those by Shibai et al. (1991) using a balloon-borne telescope revealed that the [C II] emission is bright

and ubiquitous, but the areas of these observations were very limited. The Far-Infrared Absolute Spectrophotometer (FIRAS) aboard the Cosmic Background Explorer (COBE) made the first all-sky observation of the far-infrared [C II] line (Wright et al. 1991; Bennett et al. 1994), and revealed that, on a Galactic scale, the [C II] line is the brightest emission line in the far-infrared and sub-mm wavelengths. However, the beam size of FIRAS was too large ( $7^\circ$  FWHM) to resolve detailed structures of the [C II] line emission from the Galactic plane, and it is difficult to compare the FIRAS data directly with other surveys (radio continuum, IRAS, H I, and CO) of the Galactic plane. Hence, in order to study general interstellar clouds, it has been necessary to make new [C II] line observations, which cover a significant portion of the Galactic plane with a spatial resolution comparable to those of other Galactic plane surveys made in other wavelengths.

We have made large-scale survey observations of the [C II]  $158 \mu\text{m}$  line emission from the Galactic plane using a balloon-borne telescope. Our goal is to map the entire inner Galactic plane with a sufficiently good spatial resolution ( $15'$ ) to reveal detailed structures of the Galactic plane and can be compared directly with other Galactic plane surveys. Preliminary results of our [C II] survey were discussed by Okuda et al. (1994) and by Nakagawa et al. (1995a). This paper fully describes our instrumentation, observations, and the data analysis, and presents the first results of our Galactic survey observations, which covers  $350^\circ \lesssim l \lesssim 25^\circ$  and  $|b| \lesssim 3^\circ$ . The main characteristics of the large-scale [C II] emission are also discussed briefly, but detailed interpretation of the large-scale [C II] line emission will be discussed in a later paper.

Recently, the Far-Infrared Line Mapper (FILM) on the Infrared Telescope in Space (IRTS) also made large-scale observations of the [C II] line (Shibai et al. 1996, Makiuti et al. 1996) with the spatial resolution ( $8' \times 13'$ ) similar to that of the present observations. FILM has better sensitivity than that of the present work, but, as for the Galactic plane, covers only limited areas (Murakami et al. 1996). Hence the current observation is more suitable for the systematic study of strong emission from the Galactic plane while the FILM survey can reveal much weaker emission at high Galactic latitudes. These two sets of observations are thus complementary.

## 2. INSTRUMENTATION AND OBSERVATIONS

### 2.1. Balloon-borne Infrared Carbon Explorer (BICE)

We observed the far-infrared [C II] line emission from the Galactic plane using the Balloon-borne Infrared Carbon Explorer (BICE), which is customized for large-scale, far-infrared spectroscopic observations.

The sensitivity of far-infrared observations with air-borne or balloon-borne telescopes are generally limited by photon fluctuations of atmospheric and instrumental radiation (foreground radiation). The atmospheric radiation is still very strong at airplane altitudes. At balloon altitudes, on the other hand, the atmospheric radiation is significantly reduced (Traub & Stier

1976), and the instrumental radiation generally dominates the foreground radiation. Hence, in order to achieve a good sensitivity by taking advantage of good atmospheric condition at balloon altitudes, it is essential to reduce the instrumental radiation.

When a conventional telescope at ambient temperature is used, the radiation from the telescope itself generally dominates instrumental radiation. The BICE telescope is also at ambient temperature, and, in order to reduce the instrumental radiation, we suppressed the emissivity of the telescope in two ways (see also Nakagawa 1993). First, we employed oversized optics. The physical size of the primary mirror is 35 cm, but the effective size, which is determined by a cold Lyot-stop in the spectrometer, is only 20 cm, and the outer part of the mirror is used to minimize the spill-over of radiation due to diffraction. Second, we employed an offset optics design, which removed the secondary mirror and its support from the optical path. The combination of the offset and oversized optics dramatically reduced the radiation from the telescope, and the emissivity of the telescope itself was measured to be only about 1 % at 158  $\mu\text{m}$ .

The BICE focal plane instrument is a tandem Fabry-Perot spectrometer, which consists of two Fabry-Perot interferometers: one is a high-order interferometer to scan the wavelength (Scanning Fabry-Perot, SFP), and the other is a low-order interferometer (Fixed Fabry-Perot, FFP) as an order-sorter of the SFP. The velocity resolution ( $\Delta v$ ) is 175 km s<sup>-1</sup> (FWHM). Both of the interferometers, together with other optics of the spectrometer and a far-infrared detector, are cooled to 2 K with liquid helium, and the instrumental radiation from the spectrometer is completely negligible. The detector is a stressed Ge:Ga photoconductor and is described by Hiromoto et al. (1989).

When combined with the BICE telescope, the spectrometer was designed to have a beam size of 12' (FWHM). Figure 1 shows the beam pattern obtained from laboratory measurements. We measured the beam pattern twice: once before the observations and once after the observations. The two measurements were consistent. The beam pattern can be fitted by a Gaussian with a size of 12'4 (FWHM) and an effective solid angle of  $1.5 \times 10^{-5}$  sr.

## 2.2. Fast Spectral Scanning Method

The BICE experiment is dedicated for large-scale survey observations of [C II] line emission. However, the spatial chopping method, which has been used for many infrared observations, is not suitable for large-scale observations, since signals from a reference beam could be contaminated by residual, extended emission (so-called “self-chopping”). Hence, instead of the conventional spatial chopping method, we employed a “fast spectral scanning method” to cancel the foreground radiation.

In the “fast spectral scanning method”, the signal is modulated not in the spatial domain but in the spectral domain. The modulation was achieved by continuously sweeping the SFP back and forth at 2.7 Hz in the velocity range of  $\Delta v_{\text{SCAN}} = 520$  km s<sup>-1</sup> around the expected wavelength

of the [C II] line. We determine the line intensity from the modulated signal. Moreover, from the phase of the modulation, we also obtain the central velocity of the line. Details of the data analysis are discussed in § 3.2. Since this method does not require nearby reference positions, it is suitable for mapping observations of spatially extended line emission.

### 2.3. Attitude Control

The BICE telescope is mounted on an alt-azimuth pointing system, and only the azimuthal axis is servo-controlled by driving a reaction bar. Observations were made by rotating the whole gondola around the azimuthal axis back and forth at a fixed elevation. With the diurnal motion of the sky, we were able to make a two-dimensional map of the Galactic plane. The azimuthal scan was made at a speed of  $12' \text{ s}^{-1}$  with a scan width of  $8^\circ$ . The spectral scanning was simultaneously made at 2.7 Hz as mentioned before, and thereby one spectral profile was obtained at about every one third of the beam width. We moved the elevation axis intermittently to change observing areas.

A geomagnetic aspect sensor was used as a reference of the azimuthal control. The stability of the attitude control was about  $1'$  r.m.s. when external perturbations were not severe. Since the azimuthal angle determined from the geomagnetic sensor has absolute errors as large as  $1^\circ$ , we used a visible star sensor to determine absolute positions. The uncertainty of the final position reconstruction is about  $5'$  r.m.s.

### 2.4. Observations

We made two balloon flights from the National Scientific Balloon Facility in Palestine, Texas, USA in 1991: one on May 26 and the other on June 12. In the first flight, the total emissivity which included both instrumental and atmospheric radiation, was only 3 %, but, due to some excess noise (probably electric interference), the quality of the data was not good. In the second flight, the emissivity was rather high (6 %), since the mirror had become somewhat dirty during the recovery after the first flight. However, the quality of the data was much better, and hence we concentrate on the data from the second flight in the following discussion. The system NEP during the second flight was  $6 \times 10^{-16} \text{ W Hz}^{-1/2}$ . Observation parameters are summarized in Table 1.

In the second flight, the floating altitude was 37 - 38 km and the float duration was about 8 hours. The total observation time for the Galactic plane was about 6 hours. During the same flight, we also observed the  $\rho$  Ophiuchi dark cloud (Yui et al. 1993) and the Cygnus-X region (Doi et al. 1993). In this paper, we concentrate on the Galactic plane data.

### 3. DATA ANALYSIS

#### 3.1. Foreground Radiation

We obtained more than 50,000 spectral profiles of the Galactic plane. Each spectral profile contains not only astronomical emission but also foreground radiation, which is the combination of instrumental and atmospheric radiation. In order to remove the foreground radiation and to extract astronomical emission, we assume that, at high Galactic latitudes, the astronomical emission is negligible and observed profiles contain only the foreground radiation. Figure 2 shows the observed area together with the foreground areas where we assume that astronomical emission is negligible. For comparison, we also show a far-infrared continuum emission ( $I_{\text{FIR}}$ ) map, which is calculated from the IRAS 60  $\mu\text{m}$  and 100  $\mu\text{m}$  maps (IRAS Galactic Plane Images 1986) as follows.

$$\left( \frac{I_{\text{FIR}}}{\text{erg s}^{-1} \text{ cm}^{-2} \text{ sr}^{-1}} \right) = 3.25 \times 10^{-11} \left( \frac{f_{\nu}(60\mu\text{m})}{\text{Jy sr}^{-1}} \right) + 1.26 \times 10^{-11} \left( \frac{f_{\nu}(100\mu\text{m})}{\text{Jy sr}^{-1}} \right) \quad (1)$$

This relation was originally defined for point sources (Helou et al. 1988), and we used the definition also for extended sources to represent the radiation between 40 and 120  $\mu\text{m}$ . The spatial resolution is smoothed to  $15'$ . We took the foreground areas basically as  $|b| > 3^\circ$ , but changed the areas slightly when the scan width is not enough (e.g., at  $l \approx -5^\circ$ ) or when astronomical emission extends to high latitudes (at  $l \approx 19^\circ$ ).

The average of astronomical far-infrared emission ( $I_{\text{FIR}}$ ) in the foreground areas is about  $3 \times 10^{-3} \text{ erg s}^{-1} \text{ cm}^{-2} \text{ sr}^{-1}$ , which corresponds to [C II] line emission ( $I_{[\text{CII}]}$ ) of  $2 \times 10^{-5} \text{ erg s}^{-1} \text{ cm}^{-2} \text{ sr}^{-1}$  (Here we assume  $I_{[\text{CII}]} / I_{\text{FIR}} = 6 \times 10^{-3}$ ; see §4.2). We also get  $I_{[\text{CII}]} = 2.3 \times 10^{-5} \text{ erg s}^{-1} \text{ cm}^{-2} \text{ sr}^{-1}$  at  $|b| = 3.5^\circ$  by extrapolating the FIRAS measured intensity cosecant of the high Galactic latitude ( $|b| > 15^\circ$ ) [C II] line emission (Bennett et al. 1994). In summary, our observations have a negative offset of  $I_{[\text{CII}]} \sim 2 \times 10^{-5} \text{ erg s}^{-1} \text{ cm}^{-2} \text{ sr}^{-1}$  which is comparable with our  $3\sigma$  detection limit ( $I_{[\text{CII}]} = 2 \times 10^{-5} \text{ erg s}^{-1} \text{ cm}^{-2} \text{ sr}^{-1}$ ; see §3.3). Since we concentrate on the [C II] emission from the Galactic plane with  $|b| \leq 3^\circ$ , we make no correction for this offset in most of the following discussion. This offset, however, should be taken into account, when our observations are compared with larger scale observations (§4.2).

#### 3.2. [C II] Line Emission

Each observed spectral profile was corrected for foreground radiation as described above. Since the instrumental spectral profile is much wider than intrinsic astronomical line profiles, observed spectral profiles corrected for foreground radiation are dominated by the instrumental profile. We hence fitted each observed line profile with a single Lorentzian and a linear base line. The Lorentzian profile is a good approximation for the instrumental profile. However, the observed profile is not exactly the instrumental profile; the astronomical line emission modifies the observed profiles from the instrumental profile by slightly broadening their widths and by shifting their

central positions. Taking these effects into consideration, we let the central position, the width, and the height of a Lorentzian be free parameters for the regions with strong [C II] line emission (typically  $I_{[\text{C II}]} \geq 6 \times 10^{-5} \text{ erg s}^{-1} \text{ cm}^{-2} \text{ sr}^{-1}$ ), where we can determine the three parameters accurately. We then calculated the [C II] line intensity from the fitted width and height, and derived the central velocity from the fitted central position of the Lorentzian.

On the other hand, for the regions with weak [C II] line emission (typically  $I_{[\text{C II}]} < 6 \times 10^{-5} \text{ erg s}^{-1} \text{ cm}^{-2} \text{ sr}^{-1}$ ), it is rather difficult to determine all of the three parameters of the Lorentzian independently. We hence assume that, in these regions, the [C II] line emission is dominated by radiation from the general Galactic plane. We can thus expect the central position and width of the line to be almost constant along a strip across the Galactic plane with the constant Galactic longitude. Figure 3 shows that each spatial scan is across the Galactic plane with almost constant longitude. Hence, in the regions with weak [C II] line emission, we assumed that the width and the central position was constant in each spatial scan and changed gradually from scan to scan. In each spatial scan, we calculated the mean central position and line width, both of which were weighted by line intensities, from the fitted results in the regions with strong [C II] line emission. Thus, for the regions with weak [C II] line emission, we fixed the width and the central position to the mean values in each spatial scan and fitted the height. From the fitted height and the assumed width, we calculated the line intensity.

Figure 4 shows an example of this fitting procedure for one spatial scan. This scan started at  $(l, b) = (-4^{\circ}5, -2^{\circ}8)$  and ended at  $(l, b) = (-11^{\circ}5, 3^{\circ}6)$ . The horizontal axis is the Galactic latitude. We show line intensities in Figure 4a, central positions in Figure 4b, and line widths in Figure 4c. In the region (A), where the [C II] line intensity is strong, all of the width, the velocity, and the intensity of the line were derived independently at each observed point. In the regions (B), where the [C II] line intensity is weak, only the the line intensity were derived independently at each observed point. The regions (C) correspond to the foreground areas. Flat lines in the regions (B) and (C) in Figures 4b and 4c indicate that both of the width and the velocity of the line were assumed to be constant in one scan.

The line intensities derived thereby were binned spatially into  $3'$  grids to make an intensity map. The data for grids without observations were linearly interpolated from the data in nearby bins. The map was then smoothed by a circular Gaussian with a FWHM of  $8.4'$  to remove artificial strip-like features due to the spatial scan. The final spatial resolution was broadened to  $15'$  by this smoothing.

### 3.3. Intensity Calibration

We observed M 17 as a [C II] line flux calibrator during the same flight. Matsuhara et al. (1989) obtained a two-dimensional map of the [C II] line emission from M 17. We calculated the [C II] line flux within our beam size from their map, and corrected the result for residual [C II] line

emission in the regions where they determined their baseline. The estimated [C II] line flux within our beam at the peak of M 17 is  $1.4 \times 10^{-8}$  ergs s<sup>-1</sup> cm<sup>-2</sup>. The final calibration uncertainty of the absolute intensity is about  $\pm 35$  %.

We analyzed two data sets independently; one data set was obtained when the SFP scanned from shorter to longer wavelengths (SFP-forth), and the other contains scans in the opposite manner (SFP-back). From the two independent maps thus derived, we can estimate the reliability of our data. We calculated the difference of intensity at each pixel between the two maps. Figure 5 shows the distribution of the difference. The distribution is very close to a Gaussian, and the systematic offset between the two maps are quite small ( $\Delta I_{[\text{CII}]} < 1 \times 10^{-6}$  erg s<sup>-1</sup> cm<sup>-2</sup> sr<sup>-1</sup>), which indicate that the noise is dominated by statistical fluctuations and systematic differences between the two maps are quite small. We obtained the final map by averaging the two independent data maps (§4.1), and we can also estimate the noise level of the final map from Figure 5. Since Figure 5 is the distribution of flux differences between the two maps and is dominated by statistical fluctuations, the noise level of each map is  $1/\sqrt{2}$  of that of Figure 5, and the noise level of the final averaged map is 1/2 of that of Figure 5. The detection limit of the [C II] line derived thereby is  $2 \times 10^{-5}$  erg s<sup>-1</sup> cm<sup>-2</sup> sr<sup>-1</sup> ( $3 \sigma$ ).

The uncertainty of the final intensity map is affected not only by this statistical noise but also by the uneven scanning paths of our observations. Figure 3 shows that, for most of the regions along the Galactic ridge, the step between adjacent scanning paths is smaller than a half of the beam size, which means the data were fully sampled there. However, in some regions at high latitudes (and also at a strip across the Galactic plane at  $l \approx 23^\circ$ ), the distance between adjacent scans is as large as the beam size. In these regions, the data were not fully-sampled, and peak intensities and positions of compact sources are relatively unreliable. The intensity of diffuse components is reliable to the statistical limit even in these regions.

### 3.4. Velocity Calibration

We used an atmospheric line ( $\text{O}_3$ ,  $20_8 1_2 \rightarrow 19_7 1_3$ , 157.6121  $\mu\text{m}$ ; Rothman et al. 1987) and astronomical [C II] line emission to calibrate the observed wavelength, and used M 17 and NGC 6334 as astronomical [C II] line calibration sources. The [C II] line velocity of these sources were adopted from radio observations of carbon recombination lines;  $v_{\text{LSR}} = 15.0$  km s<sup>-1</sup> for M 17 (Pankonin, Thomasson, & Barsuhn 1977) and  $v_{\text{LSR}} = -3.3$  km s<sup>-1</sup> for NGC 6334 (McGee & Newton 1981). The observed central wavelength of the [C II] line was converted to  $v_{\text{LSR}}$  following Gordon (1976). The uncertainty of the absolute velocity calibration is  $\pm 10$  km s<sup>-1</sup>.

We made velocity maps by binning the data spatially into  $12'$  grids. We applied no smoothing for the velocity data. We also analyzed two data sets (SFP-forth and SFP-back) independently, and Figure 6 shows the distribution of velocity difference at each pixel between the two data sets. The distribution is close to a Gaussian, and the systematic offset between the two maps ( $\Delta v_{\text{LSR}}$



$\approx 3 \text{ km s}^{-1}$ ) is within the uncertainty of the absolute velocity calibration. The final velocity map is the average of the two independent maps, and Figure 6 shows that the statistical uncertainty of the final velocity map is  $\pm 6 \text{ km s}^{-1}$  ( $1 \sigma$ ).

## 4. RESULTS

### 4.1. General Characteristics of [C II] Line Emission

Figure 7a shows a velocity-integrated [C II] line intensity map of the Galactic plane by false colors, and Figure 8 shows the same data in the form of a contour map. These maps were obtained by averaging the SFP-forth and SFP-back data sets as described in § 3.2. Figure 8 also shows the observed area by shade and identifications of bright sources.

As is shown in Figures 7a and 8, we have detected strong [C II] line emission from most of the area we observed. We see strong diffuse emission as well as many compact, bright sources.

Table 2 is a list of bright [C II] line ( $I_{[\text{CII}]} \geq 3 \times 10^{-4} \text{ erg s}^{-1} \text{ cm}^{-2} \text{ sr}^{-1}$ ) peaks. Column 1 is a sequential number. Columns 2 and 3 give the source peak position in Galactic coordinates. Column 4 shows the observed peak intensity. Columns 5, 6, and 7 are only for discrete sources. We assume that a [C II] line emission feature is a discrete source if the feature stood out clearly from the immediate base level with our spatial resolution. Column 5 show the base level intensity, which is the average intensity of diffuse emission around the source. Columns 6 and 7 list source sizes in Galactic longitude and latitude, respectively. The source sizes are defined as FWHM sizes of the foreground-subtracted source signals. Since the spatial distribution of the [C II] emission is rather complicated, it is difficult to define the base level intensities and the source sizes precisely. Hence they have large uncertainties, and should be treated accordingly. Column 8 gives the observed source velocity at the peak of the source (see also §4.3). Column 9 shows the source identification when it is possible.

Most of bright, compact sources correspond to young H II regions and active star-forming regions (Table 2). Tielens & Hollenbach (1985) defined photodissociation regions (PDRs) as the regions where far-ultraviolet (FUV) radiation dominates the heating of interstellar matter and determines the chemical composition of gas. Around young OB stars, dense molecular clouds are irradiated by intense radiation fields from the hot stars, and thus, warm, dense PDRs are formed. Both strong radio thermal continuum emission (e.g., Handa et al. 1987), which traces UV radiation from young OB stars, and strong CO emission (e.g., Dame et al. 1987), which traces molecular clouds, are associated with most of the bright, compact [C II] sources. Hence the [C II] line emission from these sources is attributed to the warm, dense PDRs.

On the other hand, there are some H II regions with strong [C II] line emission but with weak CO line emission. The most notable example is S 54 at  $(l, b) \approx (18^\circ.5, 2^\circ)$ . Since this is a large, evolved H II region (Johnson, Mack, & Songsathaporn 1982, Müller, Reif, & Reich 1987), we

suppose that most of molecular clouds there have been photodissociated significantly. If this is the case, we can explain the strong [C II] emission with weak CO emission. We call this type of cloud a translucent PDR (see also van Dishoeck & Black 1988; Doi et al. 1993; Nakagawa et al. 1995b).

Figure 7a also shows strong diffuse [C II] line emission, which is not directly associated with compact sources. The most promising energy source of this emission is diffuse interstellar UV radiation. Shibai et al. (1991) suggested that the diffuse [C II] emission comes from PDRs illuminated by general interstellar UV radiation. On the other hand, Heiles (1994) suggested that the extended low-density warm ionized medium (ELDWIM) was the most important candidate for the global source of the diffuse [C II] line emission. Petuchowski & Bennett (1993) argued that both of them contributed to the diffuse [C II] line emission. The origin of the diffuse [C II] line emission will be discussed in a later paper.

## 4.2. Latitudinal Profile

Figure 9 shows the latitudinal profile of the [C II] line emission together with those of H I integrated line intensity (Hartman & Burton 1997), far-infrared continuum intensity (IRAS), and CO 1-0 integrated line intensity (Dame et al. 1987). We calculated the profiles by averaging observed signals at  $5^\circ \leq l \leq 25^\circ$ . In order to get the profiles for the general Galactic plane, we excluded the Galactic center region for this estimate. We obtained far-infrared continuum intensity using equation (1), and smoothed its spatial resolution to that of the [C II] line emission ( $15'$ ). On the other hand, bin sizes of H I and CO profiles are both  $30'$ . The peak intensity of each profile is normalized to unity.

All of the profiles have their peaks around  $l \sim 0^\circ$ , but show different widths. The profiles are not simple Gaussian distributions. For simplicity, we use the FWHM measured from the base line which connects the signal at  $l = -4^\circ$  and that at  $l = 4^\circ$ . This FWHM thus shows the width of the latitudinal profile of a component at  $|b| \leq 4^\circ$ .

The latitudinal profile of the [C II] line is similar to that of the far-infrared continuum, but the FWHM of the [C II] line ( $1^\circ 32'$ ) is slightly wider than that of far-infrared continuum ( $1^\circ 18'$ ). Both of them are wider than that of the CO line ( $1^\circ 07'$ ), and are much narrower than that of H I ( $1^\circ 96'$ ). All of the above widths are observed values and are not corrected for beam sizes.

Shibai et al. (1991) also obtained latitudinal profiles of the [C II] line and other tracers of interstellar matter for one cross-cut at  $l \sim 31^\circ$  across a giant H II region W43. Since their observation covered a narrower latitude range ( $|b| < 1^\circ 2'$ ) than ours, their observed [C II] profile shows a narrower width (FWHM  $\sim 0^\circ 7'$ , W43 excluded), and is consistent with our observed profile.

Stacey et al. (1985) measured latitudinal profiles of the [C II] line emission along three cross-cuts (at  $l = 2^\circ 16'$ ,  $7^\circ 28'$ , and  $7^\circ 80'$ ) across the Galactic plane. Their observed peak intensity

at  $l = 7^{\circ}28$  ( $1.1 \times 10^{-3} \text{ erg s}^{-1} \text{ cm}^{-2} \text{ sr}^{-1}$ ) is about four times as large as our measured peak intensity ( $2.7 \times 10^{-4} \text{ erg s}^{-1} \text{ cm}^{-2} \text{ sr}^{-1}$ ) at  $l = 7^{\circ}30$ . Petuchowski et al. (1996) also measured the [C II] distribution at  $l = 7^{\circ}28$ , assuming the centroid of the distribution determined by Stacey et al. (1985). Their observed peak intensity ( $3.7 \times 10^{-4} \text{ erg s}^{-1} \text{ cm}^{-2} \text{ sr}^{-1}$ ) is consistent with our measured intensity at  $l = 7^{\circ}30$  within absolute calibration uncertainties. The FWHM of the distribution ( $43'8$ ) measured by Petuchowski et al. (1996) is also consistent with our value ( $41'2$ ), but their assumed centroid of the [C II] distribution ( $b = -15'1$ ) is clearly shifted from our observed peak position ( $b = -6'$ ). Since we measured the [C II] line distribution more directly, we believe that our measurement is more reliable than these previous measurements.

In order to obtain real scale heights, we need to know radial distribution of each emission as well as observed latitudinal distribution, and hence we have to be careful to interpret the observed latitudinal distribution alone. But the small FWHM of the [C II] line emission and its good spatial correlation with far-infrared continuum suggest that radiation from young stars is responsible for a significant fraction of the [C II] line emission.

### 4.3. Longitudinal Distribution

Figure 10 shows longitudinal distribution of the [C II] line emission observed by BICE together with the result by FIRAS (Bennett et al. 1994). We calculated the BICE [C II] distribution by integrating the observed line intensity over  $|b| \leq 3^{\circ}$  at each longitude. We also added an uniform offset of  $2.3 \times 10^{-5} \text{ erg s}^{-1} \text{ cm}^{-2} \text{ sr}^{-1}$  (see § 3.1) to the BICE result, in order to compare the distribution with that of FIRAS. The FIRAS result is integrated over  $|b| \leq 5^{\circ}$  (Bennett et al. 1994).

General profiles of the observed [C II] line emission by BICE is consistent with those of FIRAS, except for the region near the Galactic center; the [C II] peak is offset toward negative longitude by a half of the bin size in the FIRAS result. But this offset is much smaller than the beam size of FIRAS ( $7^{\circ}$ ), and the pixel quantization error is likely to be responsible for this offset.

One more thing we should note is that the relative intensity between the two measurements. The total flux measured by BICE at  $|b| \leq 3^{\circ}$  and  $350^{\circ} \leq l \leq 25^{\circ}$  is  $6.0 \times 10^{-6} \text{ erg s}^{-1} \text{ cm}^{-2}$ , while that of FIRAS at  $|b| \leq 5^{\circ}$  and the same longitudinal range is  $1.0 \times 10^{-5} \text{ erg s}^{-1} \text{ cm}^{-2}$ . Although we cannot draw a definitive conclusion here, this result suggests that BICE observations may show systematically smaller ( $\sim 65\%$ ) fluxes than FIRAS observations. It is, however, very difficult to compare the two observations directly, since (1) the effective solid angle of the both observations differ by almost three orders of magnitude, (2) we do not know the exact offset for the BICE measurement, and (3) the distribution of the [C II] line emission at  $3^{\circ} < |b| < 5^{\circ}$  is uncertain.

#### 4.4. [C II] Line Emission and Far-Infrared Continuum Emission

Since the [C II] line is the dominant coolant of the general interstellar gas, the [C II] line intensity ( $I_{\text{[C II]}}$ ) traces the heating rate of interstellar gas. The far-infrared continuum emission ( $I_{\text{FIR}}$ ), on the other hand, is a good measure of the total luminosity. Hence the  $I_{\text{[C II]}}/I_{\text{FIR}}$  ratio traces the ratio of gas heating rate to the total energy input.

In this subsection, we briefly discuss the correlation between the [C II] line emission and far-infrared continuum emission. We calculated  $I_{\text{FIR}}$  using equation (1), and in order to compare far-infrared continuum data directly with our [C II] data and also to remove zodiacal emission from the continuum data, we subtracted a certain offset from the data. We determined the offset at each longitude by linearly interpolating two data sets: one averaged over  $3^\circ < b \leq 4^\circ$  and the other over  $-4^\circ \leq b < -3^\circ$ . These regions roughly correspond to the foreground areas in Figure 2. Figure 7b shows this corrected far-infrared continuum emission, and we will use this corrected far-infrared continuum in the following discussion. The spatial resolution of Figure 7b is smoothed to that of our observation.

First, we concentrate on the general Galactic plane. Figures 7a and 7b show that the spatial correlation between the [C II] line emission and the far-infrared continuum emission is very good for the general Galactic plane; most compact sources are common for the both maps, and the distribution of diffuse components of the [C II] line emission is similar to that of far-infrared continuum emission. Figure 11 shows the intensity correlation between the two emissions; the two emissions correlate well for the general Galactic plane data, and the average  $I_{\text{[C II]}}/I_{\text{FIR}}$  ratio is about 0.6 %.

One more thing to note in Figure 11 is that the  $I_{\text{[C II]}}/I_{\text{FIR}}$  ratio has a tendency to decrease as the [C II] intensity increases; the  $I_{\text{[C II]}}/I_{\text{FIR}}$  ratio is about 0.6 % for the regions with weak [C II] line emission ( $I_{\text{[C II]}} < 1 \times 10^{-4} \text{ erg s}^{-1} \text{ cm}^{-2} \text{ sr}^{-1}$ ), but decreases to 0.4 % as the [C II] line emission becomes stronger ( $1 \times 10^{-4} < I_{\text{[C II]}} < 3 \times 10^{-4} \text{ erg s}^{-1} \text{ cm}^{-2} \text{ sr}^{-1}$ ), and reaches almost 0.2 % at the brightest end ( $I_{\text{[C II]}} > 3 \times 10^{-4} \text{ erg s}^{-1} \text{ cm}^{-2} \text{ sr}^{-1}$ ).

This situation is illustrated in a different way in Figure 7c, which shows a  $I_{\text{[C II]}}/I_{\text{FIR}}$  ratio map. In the general Galactic plane, the ratio is rather uniform on a large scale. However, we see some compact dips with  $I_{\text{[C II]}}/I_{\text{FIR}} \sim 0.2$  %. These dips correspond to bright, compact [C II] sources.

Figure 12 shows the  $I_{\text{[C II]}}/I_{\text{FIR}}$  ratio vs  $I_{60}/I_{100}$  ratio. Generally speaking, bright [C II] sources have higher  $I_{60}/I_{100}$  ratios, which mean higher UV flux densities (Hollenbach, Tielens, & Takahashi 1991). Figure 12 shows that, as the  $I_{60}/I_{100}$  ratio increases, the  $I_{\text{[C II]}}/I_{\text{FIR}}$  ratio decreases, i.e. the  $I_{\text{[C II]}}/I_{\text{FIR}}$  ratio is relatively small toward the regions with high UV flux density.

This tendency can be interpreted qualitatively on the basis of PDR models (e.g., Tielens & Hollenbach 1985; Hollenbach, Tielens, & Takahashi 1991). These model calculations show that, in high-density regions with high FUV flux density, the [C II] line intensity is rather saturated due

to its lower excitation energy and lower critical density, and other lines, such as the [O I] 63  $\mu\text{m}$  ( $^3P_1 \rightarrow ^3P_2$ ) line, become the dominant coolants. Moreover, since dust grains become positively charged in the regions with high UV flux density, the total gas heating efficiency, which is mainly due to the dust photoelectric heating, also decreases (Hollenbach, Tielens, & Takahashi 1991). The combination of these two effects decreases the  $I_{[\text{CII}]} / I_{\text{FIR}}$  ratio toward the sources with high  $I_{60} / I_{100}$  ratios.

On the other hand, the average  $I_{[\text{CII}]} / I_{\text{FIR}}$  ratio is high and has large scatter for the regions with low  $I_{60} / I_{100}$  ratios. The high ratio is attributed to the high gas heating efficiency and the dominance of the [C II] line for gas cooling. The large scatter is probably due to wide range of physical conditions in these sources.

These regions with high  $I_{[\text{CII}]} / I_{\text{FIR}}$  ratios correspond to general diffuse sources. Thus, in the [C II] line intensity map, the diffuse component is relatively bright. In other words, the intensity contrast of compact sources to diffuse components is relatively small in the [C II] line map compared to that of radio continuum maps and far-infrared continuum maps.

The FIRAS observation showed a good correlation between  $I_{[\text{CII}]}$  and  $I_{\text{FIR}'}$ , and Bennet et al. (1994) obtained a simple power law of  $I_{[\text{CII}]} \propto I_{\text{FIR}'}^{0.95}$  ( $I_{\text{FIR}'}$  is defined as the continuum intensity at the wavelength of the [C II] line). On the other hand, Figure 11 shows that we cannot fit our observed data with a simple power law; bright-[C II] regions have different correlation from that of weak-[C II] regions. For the regions with  $I_{[\text{CII}]} < 2 \times 10^{-4} \text{ erg s}^{-1} \text{ cm}^{-2} \text{ sr}^{-1}$ , we get a correlation of  $I_{[\text{CII}]} \propto I_{\text{FIR}}^{0.83}$ , which is consistent with the FIRAS result. But the correlation becomes much shallower ( $I_{[\text{CII}]} \propto I_{\text{FIR}}^{0.49}$ ) for the regions with  $I_{[\text{CII}]} \geq 2 \times 10^{-4} \text{ erg s}^{-1} \text{ cm}^{-2} \text{ sr}^{-1}$ . Since the beam size of FIRAS ( $7^\circ$ ) is much larger than typical sizes of active star-forming regions with bright [C II] line emission, we suppose that the shallower correlation between  $I_{[\text{CII}]}$  and  $I_{\text{FIR}}$  for star-forming regions is smeared out in the FIRAS measurement.

#### 4.5. Galactic Center

Next, we compare [C II] line and far-infrared continuum emissions from the Galactic center. The spatial correlation between the [C II] emission and the far-infrared continuum is worse than that for the general Galactic plane (Fig.7a and 7b). Moreover, Figure 7c shows that the Galactic center shows a clear, large dip in the  $I_{[\text{CII}]} / I_{\text{FIR}}$  map. Figure 11 shows this situation in a different way; the intensity correlation between the [C II] line emission and the far-infrared continuum emission in the Galactic center region is different from that in the general Galactic plane. As already noted by Nakagawa et al. (1995a), the  $I_{[\text{CII}]} / I_{\text{FIR}}$  ratio is about 0.2 % in the Galactic center region, and is systematically lower than that in the Galactic plane. This  $I_{[\text{CII}]} / I_{\text{FIR}}$  ratio has no correlation with the  $I_{60} / I_{100}$  ratio (Fig.12), which is again different from the tendency in the Galactic plane (see above).

Nakagawa et al. (1995a) argued that the low  $I_{[\text{CII}]} / I_{\text{FIR}}$  indicates that the abundance of the

C<sup>+</sup> ions themselves is low in the Galactic center. They attributed this low abundance mainly to soft UV radiation with fewer C-ionizing photons in the Galactic center. They also suggested that, together with the molecular self-shielding due to the high gas density, this can effectively heat molecular gas on a large scale in the Galactic center. On the basis of the relative weakness of the [C II] line emission to the CO and [C I] lines measured by FIRAS, Bennett et al. (1994) also suggested that there is an unusually large amount of well-shielded dense neutral gas in the Galactic center direction. Characteristics of the interstellar gas in the Galactic center will be discussed in a later paper.

#### 4.6. Velocity Map

Figure 13 shows the [C II] line central velocity map, which is the average of SFP-forth and SFP-back data sets (see § 3.3), together with intensity contours of the [C II] line emission. The bin size for the velocity data is 12', and we show the velocity data only in the bins where the velocities were determined successfully both in the SFP-forth and SFP-back data sets. We determined the central velocity successfully for most of the regions with  $I_{[\text{CII}]} > 6 \times 10^{-5} \text{ erg s}^{-1} \text{ cm}^{-2} \text{ sr}^{-1}$ .

Figure 13 shows a general trend that the dominant velocity component is blue-shifted in the right side and is red-shifted in the left side. This is consistent with the Galactic rotation pattern derived from other observations, such as H I 21 cm line observations (e.g., Burton 1988) and CO (1-0) line observations (e.g., Dame et al. 1987). Moreover, we also see some velocity patterns which do not match the general trend. The most notable example is the steep velocity gradient across the Galactic center;  $v_{\text{LSR}}$  is about  $-50 \text{ km s}^{-1}$  at  $l = -0^{\circ}6$  and is about  $40 \text{ km s}^{-1}$  at  $l = 0^{\circ}6$ . Spatially, the former velocity peak corresponds to Sgr C, and the latter corresponds to Sgr B<sub>2</sub>. The velocities are also consistent with the main velocity components of molecular clouds accompanying these H II regions (Bally et al. 1987). Mizutani et al. (1994) also made spectroscopic observations of the [C II] line emission from the Galactic center at  $|l| \leq 0^{\circ}7$ . The general trend of their observed velocity structures are consistent with our observed results. Although their observed area is rather limited, they have much better spatial resolution (3'.7) than ours, and they thereby revealed more detailed structures of the [C II] line emission from the Galactic center.

We also see that each discrete source has its own velocity (see also Table 2), which is different from that of the surrounding Galactic plane. For example, the velocity of M 17 ( $v_{\text{LSR}} = 15 \text{ km s}^{-1}$ ) is quite different from that of the Galactic plane ( $v_{\text{LSR}} \sim 50 \text{ km s}^{-1}$ ) at the same longitude ( $l \approx 15^{\circ}$ ). This situation is clearly illustrated also in Figure 4. The velocity of NGC 6334 ( $v_{\text{LSR}} = -5 \text{ km s}^{-1}$ ) is different from that of the nearby Galactic plane ( $v_{\text{LSR}} \approx -30 \text{ km s}^{-1}$ ). One more interesting point of Figure 4 is that the line width is narrower at NGC 6334 than at the Galactic plane. This is because there are several velocity components at the Galactic plane but there is only one dominant velocity component at each compact source such as NGC 6334.

One more thing we should mention is that, in general, clouds at high latitudes show slower

velocities than those at low latitudes. For example, at  $l = 17^\circ$ ,  $v_{\text{LSR}} \approx 50 \text{ km s}^{-1}$  at  $b = 0^\circ$ , but  $v_{\text{LSR}} \approx 35 \text{ km s}^{-1}$  at  $b = \pm 1^\circ$ . This is probably because the contribution of local components, which generally show slower velocities, is more important at higher latitudes than at lower latitudes.

#### 4.7. Longitude-Velocity Map

Figure 14a shows a longitude-velocity map of the [C II] emission, which is obtained by binning the intensities within  $|b| \leq 1^\circ$  in the longitude-velocity plane with a grid size of  $6'$  in the longitude and  $5 \text{ km s}^{-1}$  in the velocity. Please note that, since we obtain only the central velocity and cannot resolve various velocity components at each line of sight, this map is not a real longitude-velocity map but a longitude-“central velocity” map.

We can see the differential rotation pattern of our Galaxy very clearly. For comparison, we also show a position-velocity map of the CO (1-0) line emission (Dame et al. 1987) in Figure 14b. Although the instrumental velocity resolution of the BICE system ( $\Delta v = 175 \text{ km s}^{-1}$ ) is much worse than that of the CO observation ( $\Delta v = 1.3 \text{ km s}^{-1}$ ; Dame et al. 1987), the main pattern of the two diagrams are very similar. This result indicates that the “fast spectral scanning method” is very efficient to observe not only line intensities but also line velocities on a large scale.

However, there are some differences between the two position-velocity diagrams. First, we see some wavy structures in the [C II] diagram. These wavy structures correspond to the positions near bright, compact sources. For example, the wavy structure near  $l = 15^\circ$  corresponds to M 17. As was discussed above, compact sources generally have different velocities than those of the surrounding Galactic plane. When there is no bright source at a certain longitude, the emission is dominated by that from the Galactic plane, and the central velocity is that of the Galactic plane. However, if there is a bright source, the source dominates the [C II] emission in the averaged data, and the central velocity is dragged from that of the Galactic plane to that of the bright source. Thus the wavy structures are formed in the position-velocity map of the [C II] line emission (Fig.14a).

Second, the [C II] position-velocity map shows only a main structure and is simpler than the CO position-velocity map. The CO map shows many sub features, such as high velocity components around the Galactic center, and low velocity components ( $v_{\text{LSR}} \approx 0 \text{ km s}^{-1}$ ) at most of the longitudes. In the “fast spectral scanning method”, only one velocity component is assigned at each observed point, and we cannot resolve various velocity components along each line of sight. This procedure makes our [C II] position-velocity map simpler than the CO position-velocity map.

## 5. CONCLUSION

(1) We present results of our survey observations of the [C II] 158  $\mu\text{m}$  line emission from the Galactic plane. Our survey covers a wide area ( $350^\circ \lesssim l \lesssim 25^\circ$ ,  $|b| \lesssim 3^\circ$ ) with a spatial resolution (15') comparable to those of Galactic plane surveys at other wavelengths.

(2) Strong [C II] line emission was detected at almost all the areas we observed. Both compact sources and diffuse components were detected.

(3) The spatial correlation between the [C II] line emission and far-infrared continuum emission is generally good. However the diffuse component is more eminent in the [C II] line emission than in far-infrared continuum emission, and bright, compact sources show relatively small  $I_{[\text{CII}]} / I_{\text{FIR}}$  ratios.

(4) The FWHM of the latitudinal profile of the [C II] line ( $1^\circ 32'$ ) is slightly wider than that of far-infrared continuum ( $1^\circ 18'$ ). Both of them are wider than that of the CO line ( $1^\circ 07'$ ), and are much narrower than that of H I ( $1^\circ 96'$ ) line.

(5) The  $I_{[\text{CII}]} / I_{\text{FIR}}$  ratio is systematically lower in the Galactic center region on a large scale than that in the Galactic plane as noted by Nakagawa et al. (1995a)

(6) We obtained the the central velocity of the [C II] line at each observed point with strong [C II] line emission with statistical errors as small as  $\pm 6 \text{ km s}^{-1}$ . The results clearly show the differential rotation of the Galactic disk and also violent velocity fields around the Galactic center.

(7) We employed a new observing method called the “fast spectral scanning”. The method was proven to be very efficient for obtaining not only line intensities but also line velocities on a large scale.

We are indebted to the staff of the National Scientific Balloon Facility, Palestine, Texas (flight numbers 1499p and 1501p). This US-Japan collaborative project became possible through the efforts of L. J. Caroff and M. D. Bicaay at NASA headquarters. We are also grateful to N. Hiromoto for providing us with far-infrared detectors, to N. Yajima and M. Narita for their efforts in developing the BICE system, and to H. Murakami for inspiring discussions. This work was supported by grants-in-aid from Ministry of Education, Science, and Culture in Japan, and by NASA.



## REFERENCES

- Bally, J., Stark, A. A., Wilson, R. W., & Henkel, C. 1987, *ApJS*, 65, 13
- Bennett, C. L., et al. 1994, *ApJ*, 434, 587
- Burton, W. B. 1988, in *Galactic and Extragalactic Radio Astronomy*, ed. G. L. Verschuur & K. I. Kellermann (Berlin: Springer), 295
- Cooksey, A. L., Blake, G. A., & Saykally, R. J. 1986, *ApJ*, 305, L89
- Dalgarno, A., & McCray, R. A. 1972, *ARA&A*, 10, 375
- Dame, T. M., et al. 1987, *ApJ*, 322, 706
- Doi, Y., Nakagawa, T., Yui, Y. Y., Okuda, H., Shibai, H., Nishimura, T., & Low, F. J. 1993, in *Back to the Galaxy*, ed. S. S. Holt & F. Verter (New York: AIP), 307
- Gordon, M. A. 1976, in *Methods of Experimental Physics, Vol.12, Astrophysics, Part C, Radio Observations*, ed. M. L. Meeks (New York: Academic Press), 277
- Haas, M. R., Davidson, J. A., & Erickson, E. F. 1995, *Airborne Astronomy Symposium on the Galactic Ecosystem: From Gas to Stars to Dust* (San Francisco: ASP)
- Handa, T., Sofue, Y., Nakai, N., Hirabayashi, H., & Inoue, M. 1987, *PASJ*, 39, 709
- Hartmann, D. & Burton, W. B. 1997, *Atlas of Galactic Neutral Hydrogen* (Cambridge: Cambridge University Press)
- Heiles, C. 1994, *ApJ*, 436, 720
- Helou, G., Khan, I. R., Malek, L., & Boehmer, L. 1988, *ApJS*, 68, 151
- Hiromoto, N., Itabe, T., Aruga, T., Okuda, H., Matsuhara, H., Shibai, H., Nakagawa, T., & Saito, M. 1989, *IR Physics*, 29, 255
- Hollenbach, D., Tielens, A. G. G. M., & Takahashi, T. 1991, *ApJ*, 377, 192
- IRAS Catalogs and Atlases: Explanatory Supplement (NASA RP-1190) 1988, ed. C. A. Beichman, G. Neugebauer, H. J. Habing, P. E. Clegg, & T. J. Chester (Washington, DC: GPO)
- IRAS Galactic Plane Images 1986, as described in IRAS Explanatory Supplement 1988
- Johnson, P. G., Mack, P., & Songsathaporn, R. 1982, *Ap&SS*, 86, 331
- Makiuti, S., Okuda, H., Shibai, H., Nakagawa, T., Matsuhara, H., Hiromoto, N., & Okumura, K. 1996, *PASJ*, 48, L71
- Matsuhara, H., et al. 1989, *ApJ*, 339, L67

- McGee, R. X., & Newton, L. M. 1981, *MNRAS*, 196, 889
- Mizutani, K., et al. 1994, *ApJS*, 91, 613
- Müller, P., Reif, K., & Reich, W. 1987, *A&A*, 183, 327
- Murakami, H. et al. 1997, *PASJ*, 48, L41
- Nakagawa, T. 1993, in *Astronomical Infrared Spectroscopy: Future Observational Directions*, ed. S. Kwok (San Francisco: ASP), 373
- Nakagawa, T., et al. 1995a, *ApJ*, 455, L35
- Nakagawa, T., et al. 1995b, in *The Physics and Chemistry of Interstellar Molecular Clouds*, ed. G. Winnewisser & G. C. Pelz (Berlin: Springer), 22
- Okuda, H., et al. 1994, *IR Physics*, 35, 391
- Pankonin, V., Thomasson, P., & Baruhn, J. 1977, *A&A*, 54, 335
- Petuchowski, S. J. & Bennett, C. L. 1993, *ApJ*, 405, 591
- Petuchowski, S. J. Bennett, C. L., Haas, M. R., Colgan, W. J., & Erickson, E. F. 1996, *ApJ*, 459, 181
- Rothman, L. S., et al. 1987, *Appl. Opt.*, 26, 4058
- Shibai, H., et al. 1991, *ApJ*, 374, 522
- Shibai, H., Okuda, H., Nakagawa, T., Makiuti, S., Matsuhara, H., Hiromoto, N., & Okumura, K. 1996, *PASJ*, 48, L127
- Stacey, G., Viscuso, P. J., Fuller, C. E., & Kurtz, N. T. 1985, *ApJ*, 289, 803
- Tielens, A. G. G. M., & Hollenbach, D. 1985, *ApJ*, 291, 722
- Traub, W. A., & Stier, M. A. 1976, *Appl. Opt.*, 15, 364
- van Dishoeck, E. F., & Black, J. H. 1988, *ApJ*, 334, 771
- Wright, E. L., et al. 1991, *ApJ*, 381, 200
- Yui, Y. Y., Nakagawa, T., Doi, Y., Okuda, H., Shibai, H., Nishimura, T., & Low, F. J. 1993, *ApJ*, 419, L37

Fig. 1.— Beam profiles measured in the laboratory. Filled circles show measured data points and curves show fitted Gaussian profiles with FWHM of  $12''.4$ .

Fig. 2.— The observed area is shown by shades; the dark shade indicates the area where the observed data are valid, and the light shade shows the area which we used to determine foreground radiation. For comparison, far-infrared continuum flux (IRAS, see text) is shown by contours; their levels are 0.3, 0.5, 1, 2, 4, 8, 15, 30, and  $60 \times 10^{-2} \text{ erg s}^{-1} \text{ cm}^{-2} \text{ sr}^{-1}$ .

Fig. 3.— Scan paths.

Fig. 4.— Example of the data analysis for one spatial scan. This scan started at  $(l, b) = (-4^\circ 5', -2^\circ 8')$  and ended at  $(l, b) = (-11^\circ 5', -3^\circ 6')$ . The horizontal axis is the Galactic latitude. Figure 4a shows the line intensity, Figure 4b shows  $v_{\text{LSR}}$  derived from the line central position, and Figure 4c shows the line width. In the region (A), where the [C II] line intensity is strong, the width, velocity, and intensity of the line were derived at each observed point. In the regions (B), where [C II] line intensity is weak, only the line intensity was derived independently at each observed point. Flat lines in Figure 4b and Figure 4c indicate that both the width and the velocity of the line were assumed to be constant in one spatial scan (see text). The regions (C) are the areas where we determined foreground radiation.

Fig. 5.— The difference of intensities between the SFP-forth data set and the SFP-back data set. Each data set was binned into  $3'$  grids and smoothed to a spatial resolution of  $15'$  (FWHM). The solid curve shows a fitted Gaussian profile with  $\sigma = 1.4 \times 10^{-5} \text{ erg s}^{-1} \text{ cm}^{-2} \text{ sr}^{-1}$ .

Fig. 6.— The difference of velocities between the SFP-forth data set and the SFP-back data set. Each data set was binned into  $12'$  grids, and no smoothing was made. This figure contains only the data point in the areas which correspond to the region (A) in Figure 4. The solid curve shows a fitted Gaussian profile with  $\sigma = 12 \text{ km s}^{-1}$ .

Fig. 7.— (a) Far-infrared [C II] line intensity map ( $I_{[\text{CII}]}$ ) obtained by BICE. (b) Far-infrared continuum map ( $I_{\text{FIR}}$ ) obtained from IRAS 60 and  $100 \mu\text{m}$  maps. Offsets are subtracted (see the text). (c) The ratio of the far-infrared [C II] line emission to the far-infrared continuum emission ( $I_{[\text{CII}]} / I_{\text{FIR}}$ ). The spatial resolutions of the three maps are  $15'$ .

Fig. 8.— Far-infrared [C II] line intensity contour map obtained by BICE with the spatial resolution of  $15'$ . Contour Levels are 0.3, 0.6, 1, 1.5, 2, 3, 4, 6, and  $9 \times 10^{-4} \text{ erg s}^{-1} \text{ cm}^{-2} \text{ sr}^{-1}$ . The shade shows the observed area. Representative bright sources are labelled.

Fig. 9.— Latitudinal profile of the [C II] line emission together with those of H I line (Hartman & Burton 1997), far-infrared continuum (IRAS), and CO 1-0 line (Dame et al. 1987). The profiles are averaged at  $5^\circ \leq l \leq 25^\circ$ . The spatial resolutions of the [C II] line emission and far-infrared continuum profiles are  $15'$ , and bin sizes of H I and CO profiles are  $30'$ . Peak intensities are normalized, and offsets (values indicated in parentheses) are added for clarity.

Fig. 10.— Longitudinal distribution of the [C II] line emission observed by BICE ( $|b| \leq 3^\circ$ ) together with that by FIRAS ( $|b| \leq 5^\circ$ ) (Bennett et al. 1994). We added an uniform offset of  $2.3 \times 10^{-5}$  erg  $\text{s}^{-1} \text{cm}^{-2} \text{sr}^{-1}$  to the BICE result (see text).

Fig. 11.— Intensity correlation between the far-infrared [C II] line emission and the far-infrared continuum emission. Each point shows a data for a  $15'$  pixel. Open circles are for the Galactic center ( $-4^\circ \leq l \leq 5^\circ, |b| \leq 1^\circ$ ), and small dots are for the Galactic plane. The upper and lower lines show  $I_{[\text{CII}]} / I_{\text{FIR}} = 6 \times 10^{-3}$  and  $2 \times 10^{-3}$ , respectively.

Fig. 12.— Relation between the  $I_{[\text{CII}]} / I_{\text{FIR}}$  ratio and the far-infrared color  $I_{60} / I_{100}$ . Each point shows data for a  $15'$  pixel with  $I_{\text{FIR}} \geq 1 \times 10^{-2}$  erg  $\text{s}^{-1} \text{cm}^{-2} \text{sr}^{-1}$ . Open circles are for the Galactic center ( $-4^\circ \leq l \leq 5^\circ, |b| \leq 1^\circ$ ), and small dots are for Galactic plane.

Fig. 13.— Velocity map of the far-infrared [C II] line emission with a pixel size of  $12'$ . The intensity of the [C II] is also shown by contours with the levels of 1, 2, 4, and  $8 \times 10^{-4}$  erg  $\text{s}^{-1} \text{cm}^{-2} \text{sr}^{-1}$ .

Fig. 14.— (a) Longitude-velocity map of the far-infrared [C II] line emission. This is obtained by averaging the velocity data weighted by intensities at each longitude within  $|b| \leq 1^\circ$ . The results are binned by  $6'$  in the longitude and  $5 \text{ km s}^{-1}$  in the velocity. (b) [C II] longitude-velocity map (contours, this work) superposed on a CO longitude-velocity map (false colors, Dame et al. 1987). The resolution of the CO data is  $30'$  in longitude and  $1.3 \text{ km s}^{-1}$  in velocity.

Table 1. Observation Parameters

parameter	value
Target Line	[C II], $^2P_{3/2} \rightarrow ^2P_{1/2}$ , 157.7409 $\mu\text{m}$
Spatial Resolution	12'4 (FWHM) (beam size) 15' (FWHM) (final map)
NEP <sub>sys</sub>	$6 \times 10^{-16} \text{ W Hz}^{-1/2}$
Detection Limit	$2 \times 10^{-5} \text{ ergs s}^{-1} \text{ cm}^{-2} \text{ ster}^{-1}$ ( $3\sigma$ )
Velocity Resolution	175 km s <sup>-1</sup> (FWHM)
Velocity Determination	$\pm 6 \text{ km s}^{-1}$ ( $1\sigma$ )
Intensity Calibration	[C II] line map of M 17 by Matsuhara et al. (1989)
Intensity Calibration Uncertainty	$\pm 35 \%$
Observed Region	$350^\circ \lesssim l \lesssim 25^\circ$ , $ b  \lesssim 3^\circ$

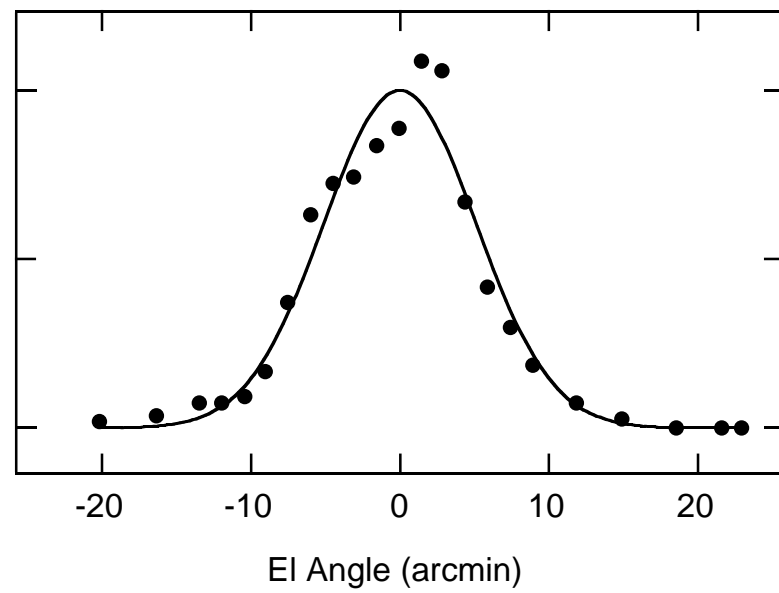
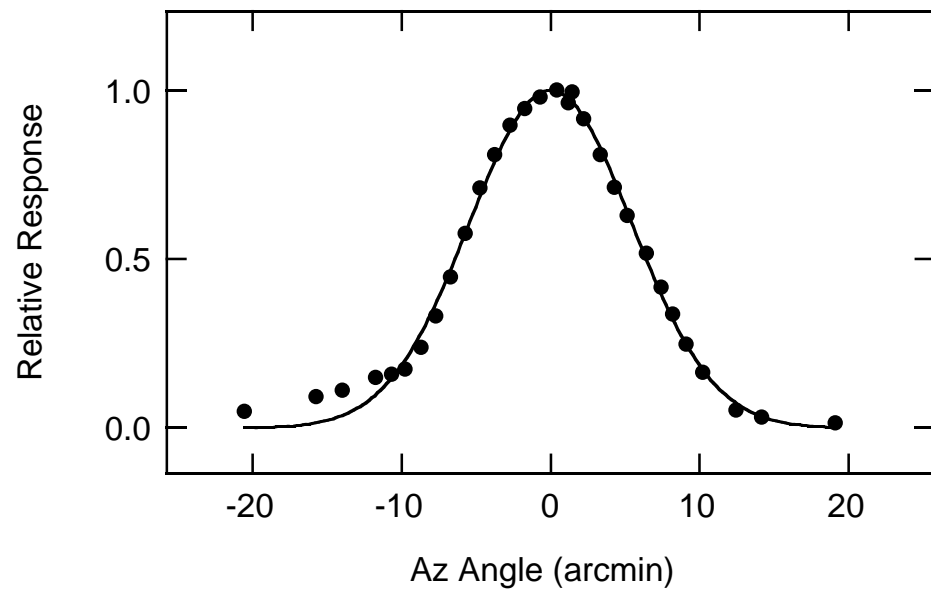
Table 2. Bright Peaks

No	$l$ ( $^{\circ}$ )	$b$ ( $^{\circ}$ )	peak intensity <sup>a</sup>	base level <sup>a</sup>	$\Delta l$ ( $'$ )	$\Delta b$ ( $'$ )	$v_{\text{LSR}}$ ( $\text{km s}^{-1}$ )	identification
1	351.30	0.70	9.07	1.20	29	23	-5	NGC 6334
2	353.20	0.70	6.10	1.00	26	37	5	NGC 6357
3	353.55	0.00	3.39	1.83	16	15	-34	
4	0.05	0.00	12.02	6.90	15	19	-4	Sgr A
5	5.90	-0.40	3.83	2.20	17	18	10	
6	5.95	-1.15	4.59	1.50	20	31	11	M 8
7	6.60	-0.20	3.45	2.65	15	16	21	
8	7.05	-0.20	3.37	2.65	15	15	16	M 20
9	8.15	0.00	3.12	2.30	19	15	42	
10	8.60	-0.30	3.81	2.60	24	28	30	W 30
11 <sup>b</sup>	10.40	0.00	3.24	...	...	...	7	
12	10.70	-0.35	3.66	2.70	17	15	8	
13	12.80	-0.20	3.91	2.10	19	19	27	
14	14.00	-0.10	3.32	2.56	29	15	37	
15 <sup>b</sup>	14.10	-0.55	3.04	...	...	...	30	
16	15.10	-0.70	8.71	1.50	25	20	15	M 17
17	16.40	0.05	3.55	2.55	17	24	46	
18 <sup>b</sup>	16.45	-0.20	3.16	...	...	...	43	
19	17.10	0.90	4.59	1.40	23	34	32	M 16
20	18.20	-0.25	4.49	2.60	16	18	51	
21	18.15	2.00	3.51	0.53			35	
22	18.40	2.00	3.48	0.52	} 33	29	35	} S 54, W 35
23	18.75	2.00	3.36	0.49			26	
24	19.05	-0.40	4.94	2.60	22	37	62	
25	19.60	-0.10	3.16	1.95	23	20	60	
26	20.75	-0.10	3.07	1.60	20	18	62	
27 <sup>c</sup>	22.30	-0.20	3.35	...	...	...	83	
28 <sup>c</sup>	23.00	-0.35	4.62	...	...	...	71	
29	23.80	0.10	4.11	3.15	21	15	91	
30 <sup>c</sup>	24.60	-0.10	5.61	...	...	...	88	

<sup>a</sup>The unit is  $10^{-4} \text{ erg s}^{-1} \text{ cm}^{-2} \text{ sr}^{-1}$ .

<sup>b</sup>These sources are parts of diffuse emission, and we cannot determine their base levels and source sizes.

<sup>c</sup>These sources are at the edge of scanned areas, and part of the sources are out of our observed range. Hence base levels and source sizes cannot be determined precisely. The true peaks may be out of our observed area and their intensities are also uncertain. The peak intensities listed above are those within our surveyed areas.



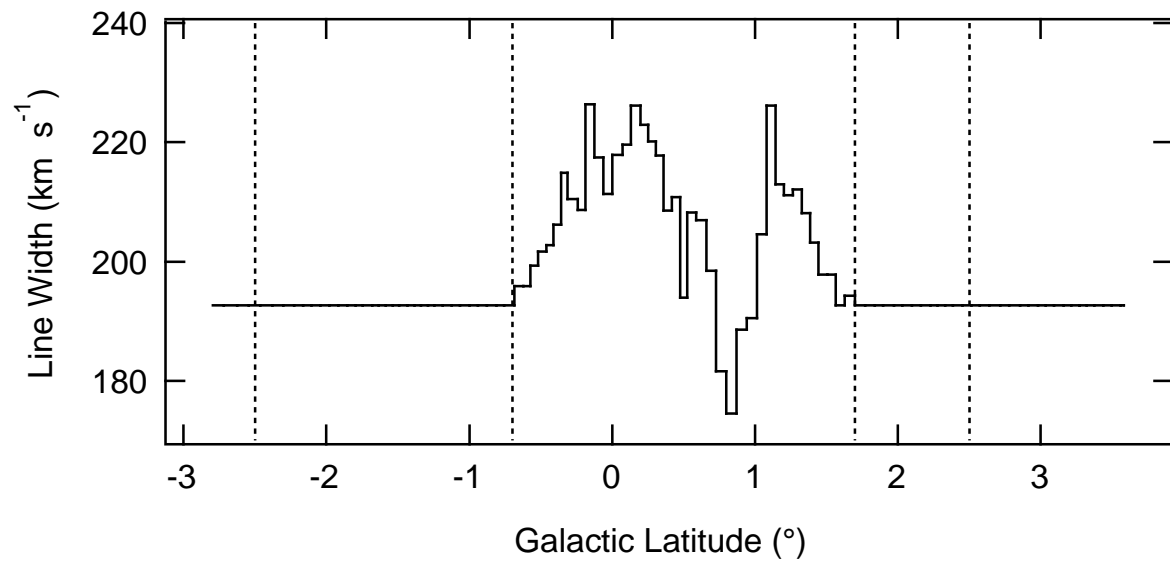
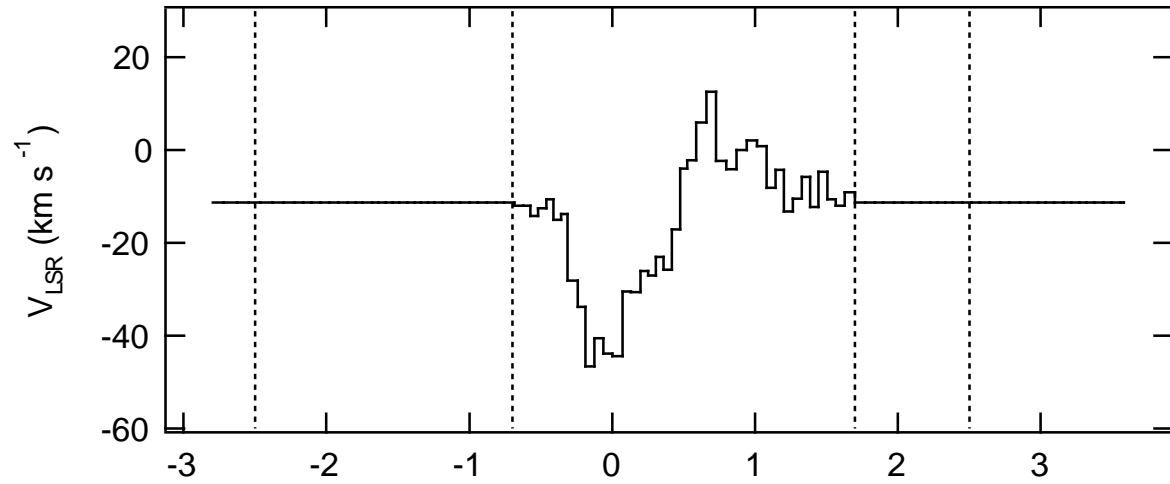
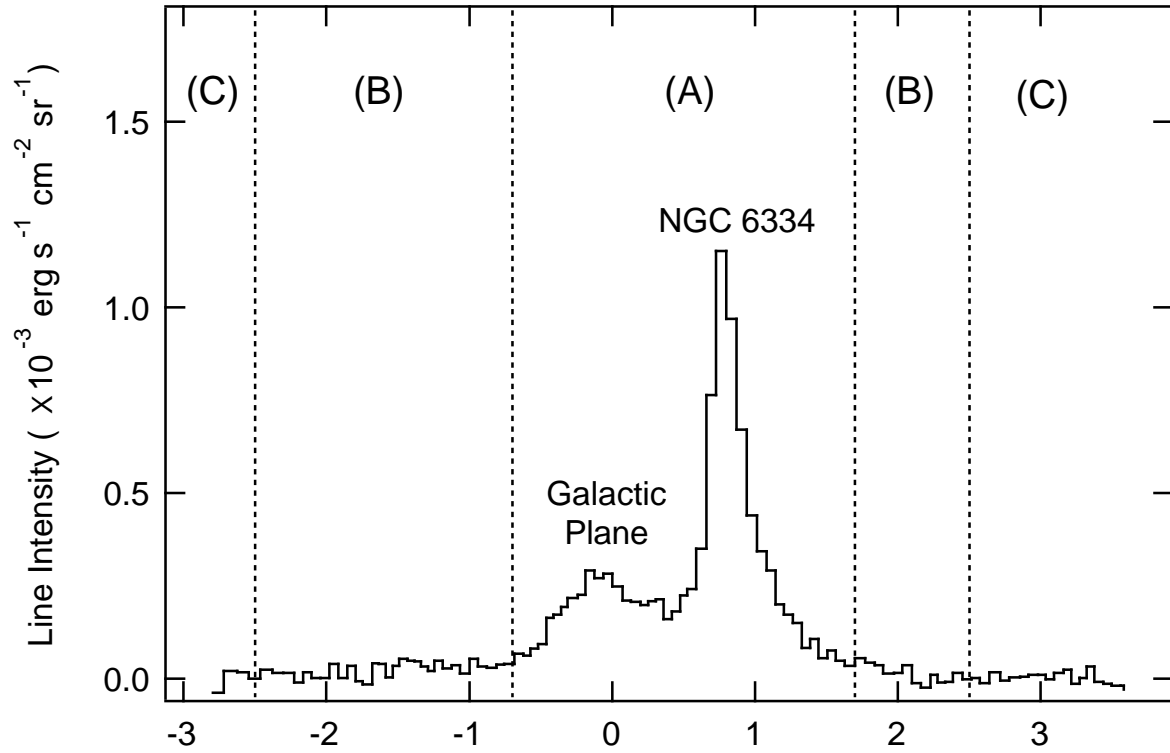
This figure "fig2.jpg" is available in "jpg" format from:

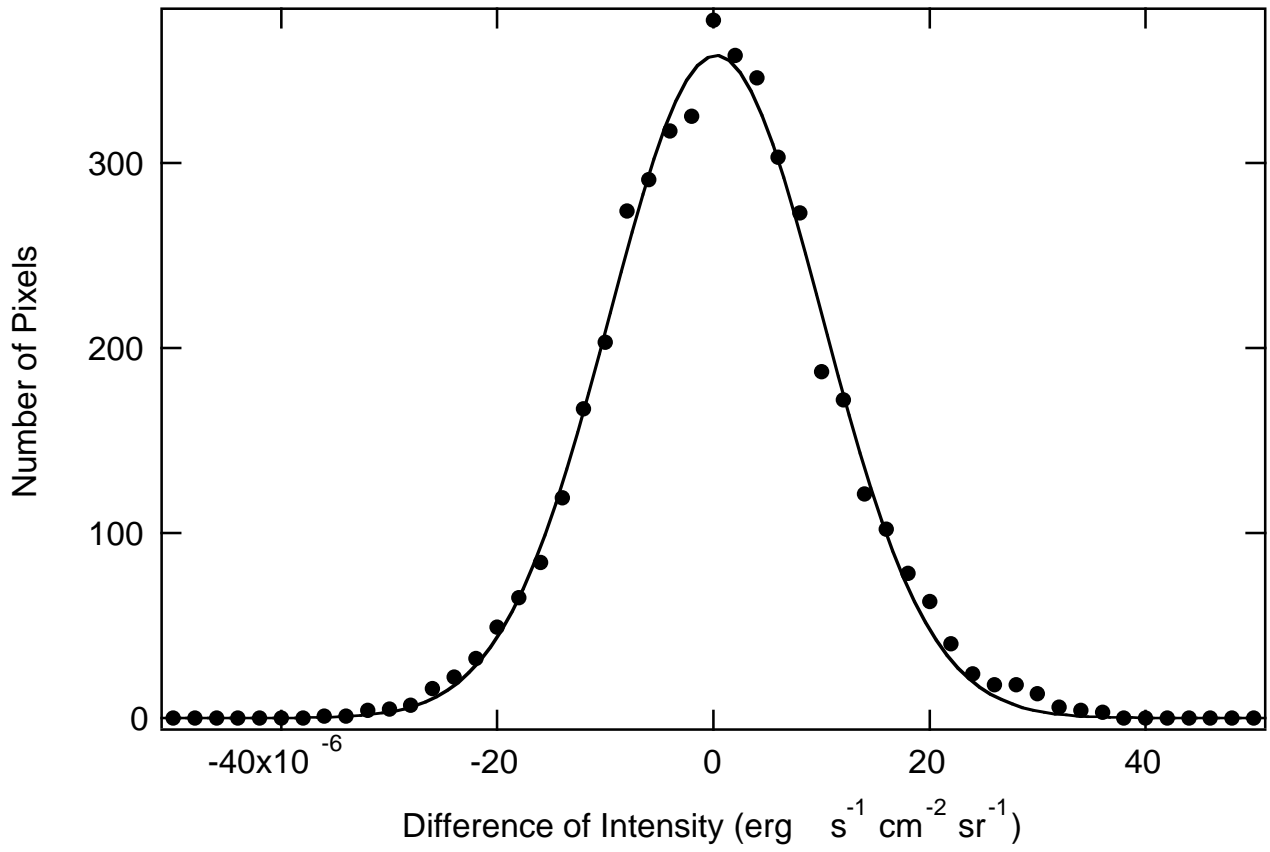
<http://arxiv.org/ps/astro-ph/9712333v1>

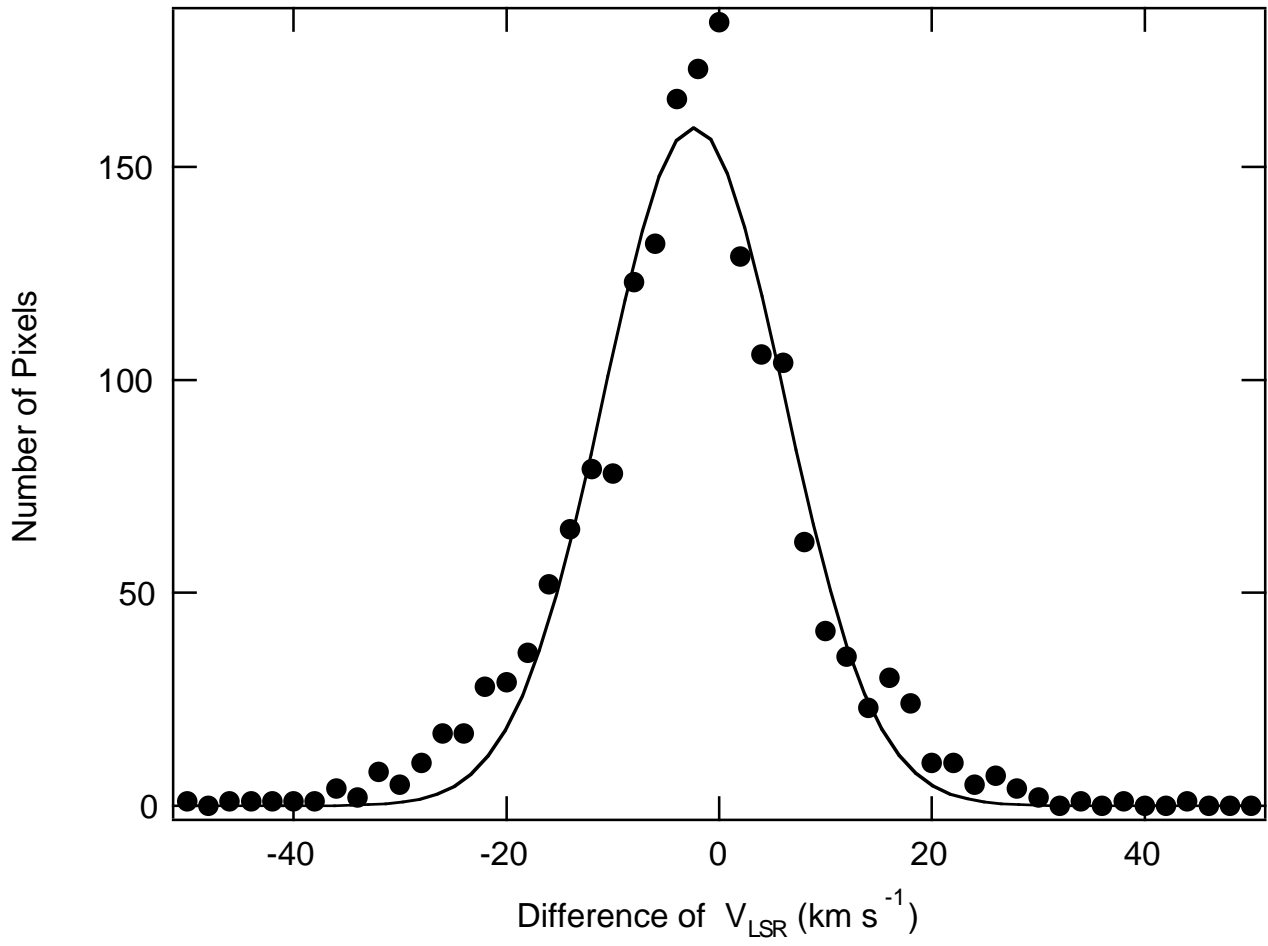


This figure "fig3.jpg" is available in "jpg" format from:

<http://arxiv.org/ps/astro-ph/9712333v1>





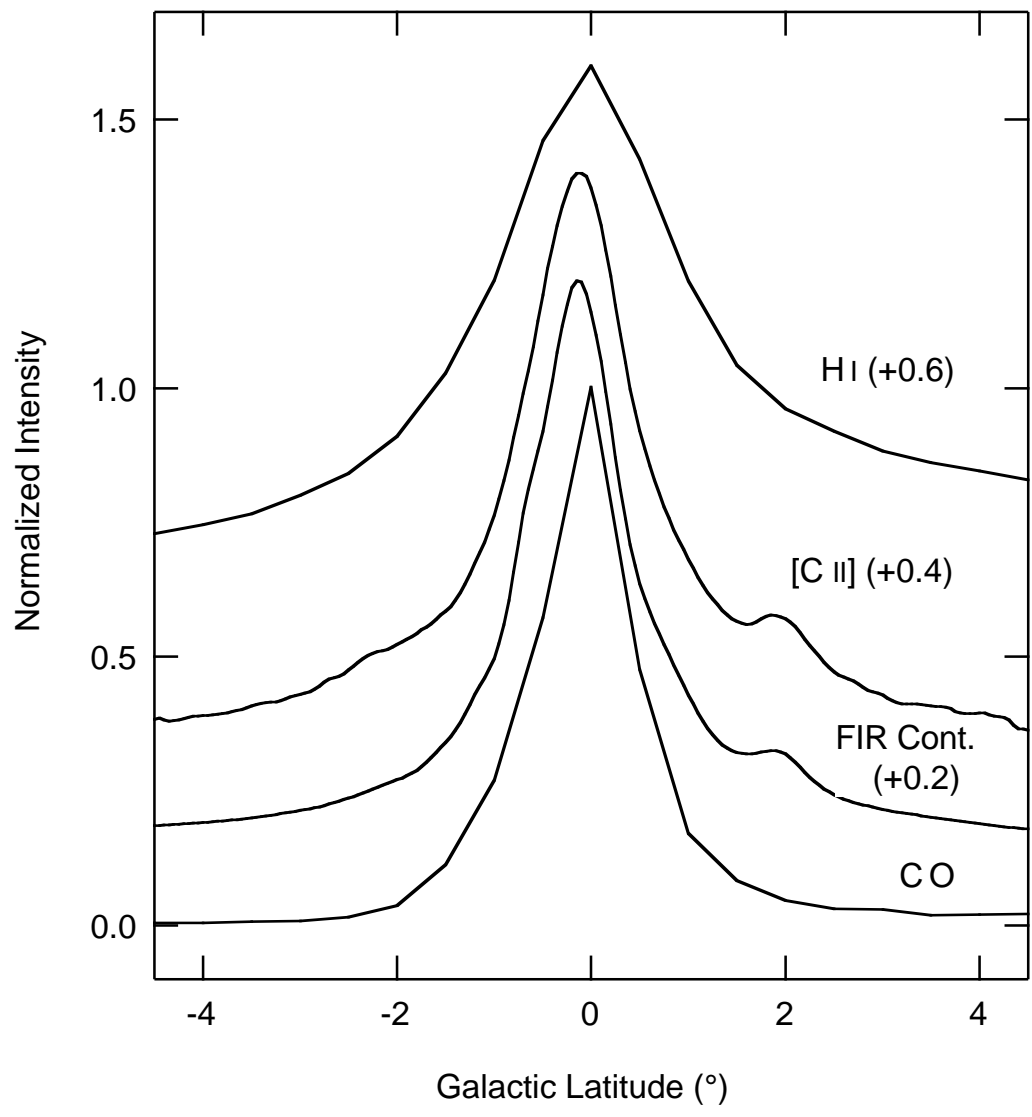


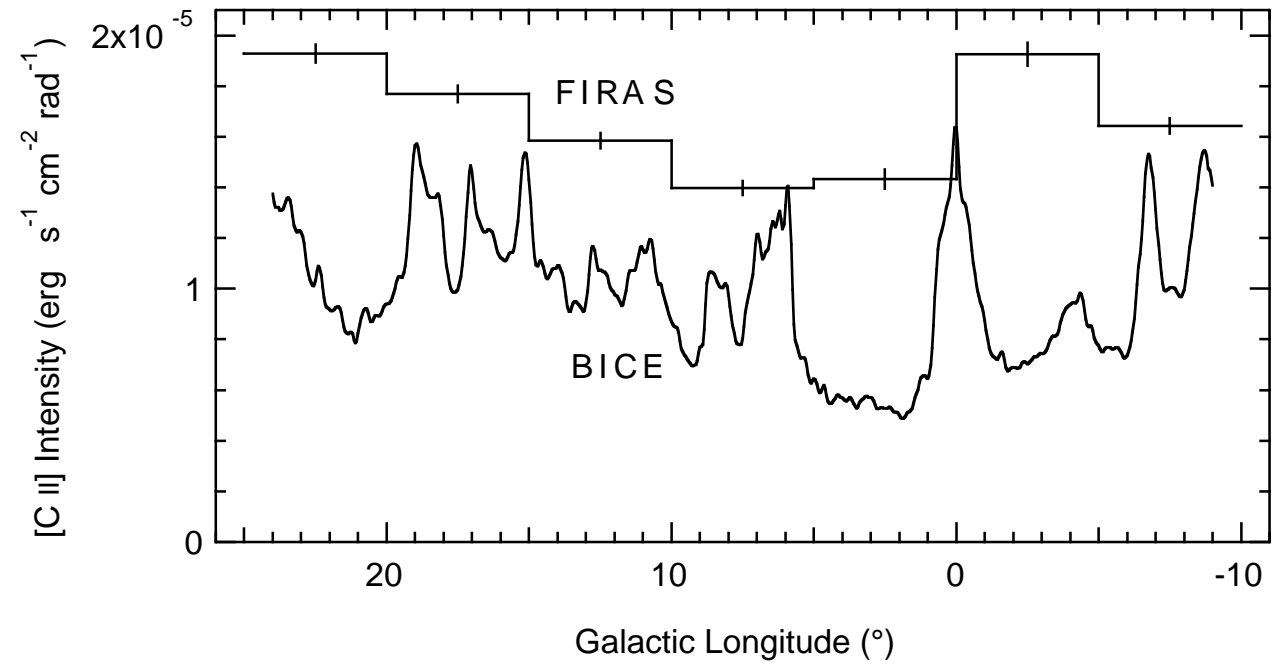
This figure "fig7.jpg" is available in "jpg" format from:

<http://arxiv.org/ps/astro-ph/9712333v1>

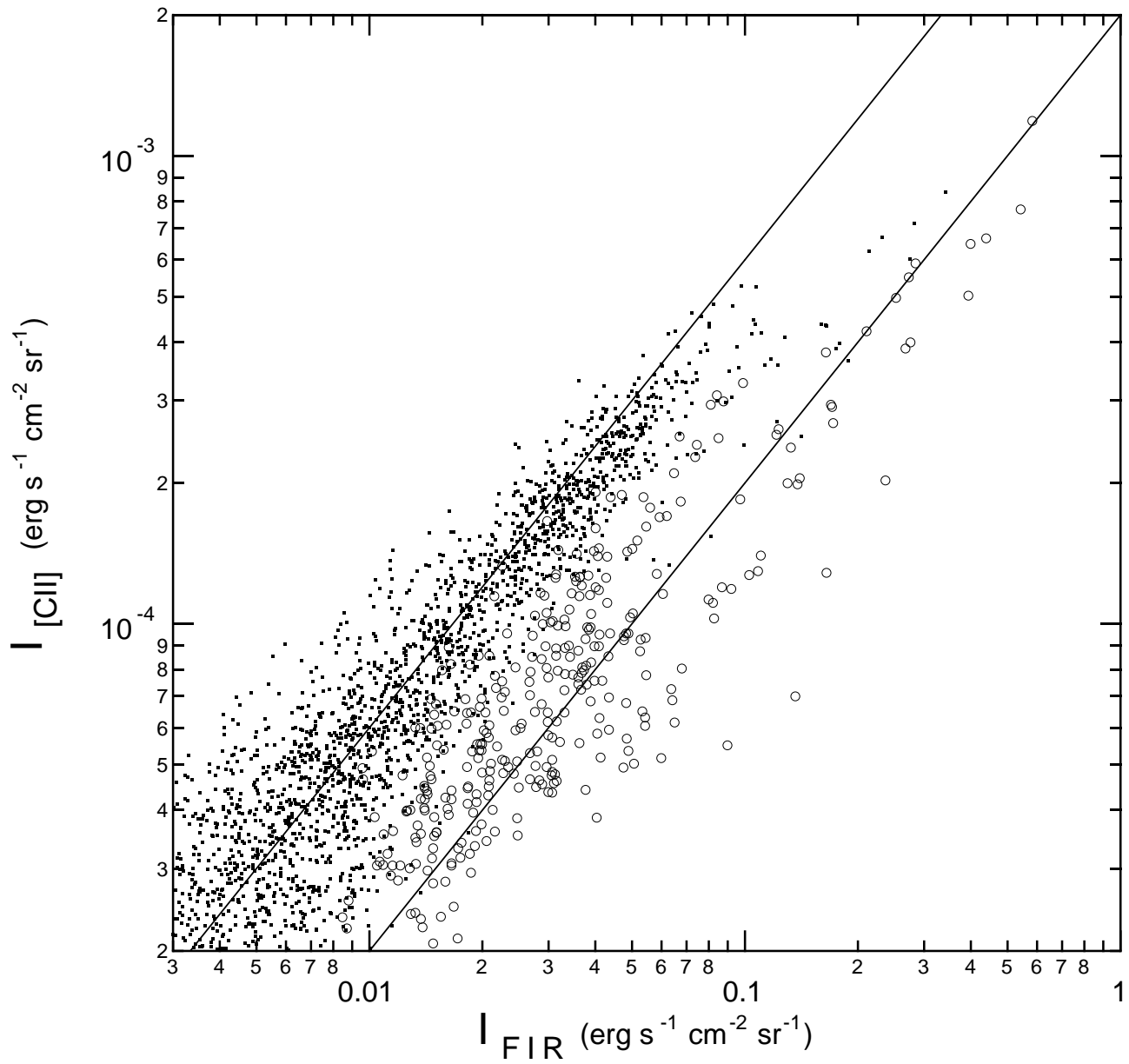
This figure "fig8.jpg" is available in "jpg" format from:

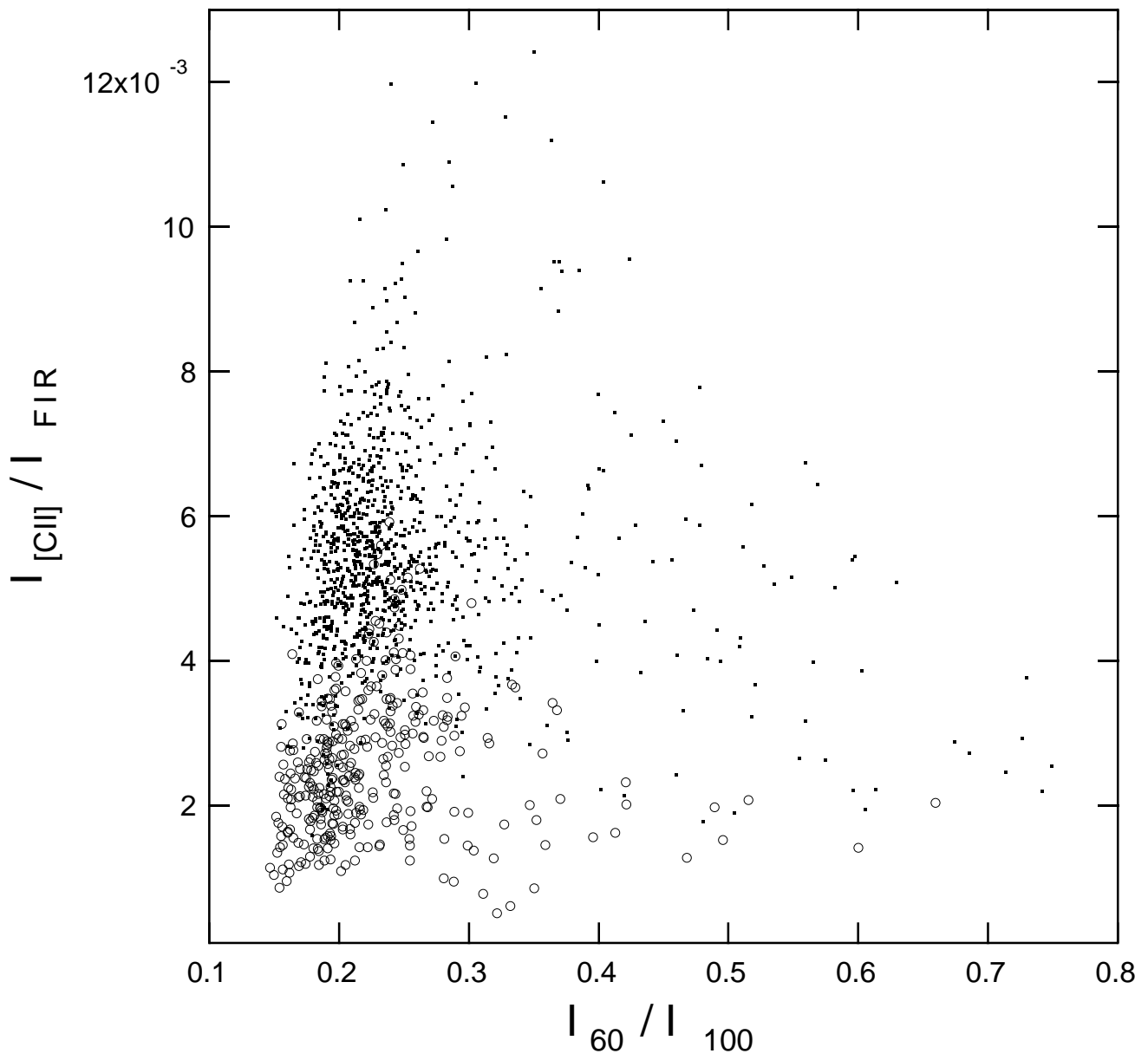
<http://arxiv.org/ps/astro-ph/9712333v1>











This figure "fig13.jpg" is available in "jpg" format from:

<http://arxiv.org/ps/astro-ph/9712333v1>

This figure "fig14.jpg" is available in "jpg" format from:

<http://arxiv.org/ps/astro-ph/9712333v1>